Efficiency of room acoustic simulations with time-domain FEM including frequency-dependent absorbing boundary conditions: Comparison with frequency-domain FEM

Okuzono, Takeshi
Yoshida, Takumi
Sakagami, Kimihiro

(Citation)
Applied Acoustics,182:108212

(Issue Date)
2021-11

(Resource Type)
journal article

(Version)
Accepted Manuscript

(URL)
https://hdl.handle.net/20.500.14094/90008379

Efficiency of room acoustic simulations with time-domain FEM including frequency-dependent absorbing boundary conditions: Comparison with frequency-domain FEM

Takeshi Okuzono[a,1] Takumi Yoshida[a,b] and Kimihiro Sakagami[a]

[a] *Environmental Acoustic Laboratory, Department of Architecture, Graduate School of Engineering, Kobe University, 1-1, Rokkodai, Nada, Kobe 657-8501, Japan*

[b] *Technical Research Institute, Hazama Ando Corporation, Tsukuba 305-0822, Japan*

Abstract

Recent wave-based room acoustic simulations in the time domain can incorporate frequency-dependent absorbing boundary conditions (BCs), by which time responses including a broad frequency component are calculable with a single computational run. However, their performance over the frequency-domain method remains poorly understood. This paper presents a discussion of the capabilities of a recently developed implicit time-domain finite element method (TD-FEM) for room acoustics simulation by comparison with a fourth-order accurate frequency-domain FEM (FD-FEM). First, the implicit TD-FEM accuracy is examined via an impedance tube problem, having frequency-dependent absorbing BCs at the tube end, where a specific acoustic admittance ratio of rigidly backed porous sound absorbers is imposed. Results indicate that the implicit TD-FEM has the same solution convergence rate as that of FD-FEM. The solution converges to the FD-FEM solution when using a sufficiently small time interval. A performance comparison of both methods is then made using two real-scale 2D room acoustic problems in an office room and a complexly shaped concert hall. Numerical

[1] Corresponding author. Tel./fax: +81 78 803 6577.
E-mail address: okuzono@port.kobe-u.ac.jp (T. Okuzono).

results show that the implicit TD-FEM can be useful for acoustic simulation in practical-sized rooms at broad frequency ranges with markedly smaller computational costs than those of FD-FEM while maintaining similar accuracy.

Keywords: Acoustic simulations, Finite element method, Frequency-dependent impedance boundary, Porous sound absorber, Wave-based room acoustic modeling

1. Introduction

Wave-based acoustic solvers, solving the Helmholtz equation or wave equation with numerical methods, are physically reliable prediction methods of room acoustics. With these solvers, one can accurately consider boundary effects such as sound absorption and sound scattering. Although wave-based simulations are still expensive as a room acoustic design tool, especially for real-sized rooms at kilohertz frequency ranges, their applicability has continued to expand gradually in both frequency and time domains with the advance of recent computer technology, e.g., [1, 2, 3, 4, 5]. In room acoustic simulations, calculating the room impulse responses is fundamentally important to evaluate room acoustics using acoustical parameters such as reverberation times and clarity [6]. Visualization of sound propagation inside rooms and auralization of the sound field is also helpful for acoustic evaluation. Therefore, time-domain wave-based solvers, which calculate an impulse response straightforwardly in the time domain, are very attractive. Various solvers have been developed to date. The representative solvers are the following: The finite-difference time-domain (FDTD) method [1, 7, 8, 9, 10, 11, 12], the time-domain finite element method (TD-FEM) [3, 13, 14, 15, 16, 17, 18], the finite volume time-domain method [19, 20], the pseudospectral time-domain method [21, 22], the discontinuous Galerkin FEM [23, 24, 25, 26], the spectral element method [27], and the adaptive rectangular decomposition method [28, 29]. Time-domain solvers have inherent difficulty in accommodating frequency-dependent quantities such as the specific acoustic impedance of sound absorbers, but recent developments have enabled us to consider it for some sound absorbers such as porous absorbers [1, 18, 19, 25, 27, 29]. Therefore, recent time-domain solvers are becoming able to perform acoustics simulations considering a frequency-dependent absorbing boundary at wideband frequencies. The study described herein specifically addresses

such a recently developed room acoustic solver with TD-FEM, among others, and presents discussion of its performance in comparison with frequency-domain FEM (FD-FEM), which can exactly reflect the frequency-dependence of an absorbing boundary.

The TD-FEM [15, 18] proposed by the authors discretizes the weak form of the wave equation with dispersion-reduced finite elements [30] in the spatial domain. The semi-discretized equation is solved by application of an efficient direct time integration method: Fox–Goodwin method [31, 32]. The resulting time-marching scheme uses a preconditioned iterative solver [33] for the linear system solution at each time step. The inherent benefit of TD-FEM is its capability of dealing with complex geometries. Despite its simple implementation with low-order elements, by virtue of the use of the dispersion reduction technique called the modified integration rules [30], the authors' formulation has fourth-order accuracy in an idealized case with respect to dispersion error: the error in sound speed. Dispersion error reduction is based on minimization of the dispersion error via dispersion error analysis assuming free field sound propagation. Furthermore, by virtue of the rapid convergence of iterative solver, the computational costs are low in spite of the implicit formulation. Its applicability to practical acoustic simulations has been demonstrated via acoustic simulation in a simple-shaped 3D concert hall and a full-scale simulation of reverberation absorption coefficient measurement with frequency-independent boundary conditions (BCs) and an extended-reaction model of permeable membranes [34, 3]. In very recent years, frequency-dependent impedance BCs are implemented further assisted by the auxiliary differential equation (ADE) method [35, 36] for efficient computation of convolutions [18]. The validity of the implementation was demonstrated via an impedance tube problem in which sound absorption characteristics of a rigid-backed glass-wool absorber calculated using TD-FEM were compared with results obtained using the transfer matrix method. Nevertheless, discretization error characteristics included in TD-FEM and performance compared to FD-FEM remain unclear.

Acoustic simulations using FEM usually perform in the frequency domain [37, 38, 39]. Such simulations can calculate the room's impulse responses with the inverse Fourier transform [40, 5]. However, for room acoustic simulation dealing with a large-scale 3D sound field and wideband frequencies, FD-FEM is quite time-consuming for computation of impulse responses because of the inherent difficulty in solving a linear system of equations efficiently with many degrees of freedom (DOF), especially for high frequen-

cies [37, 38, 40]. However, TD-FEM can solve sizable linear systems quickly at each time step with the iterative solver [3, 14, 15, 16]. Therefore, for predicting sound fields with many DOF, TD-FEM has a possibility of accomplishing the task more rapidly than FD-FEM can. Further performance improvement can be expected because TD-FEM can be formulated as an explicit solver [17].

The present study was undertaken to elucidate the implicit TD-FEM performance against fourth-order accurate FD-FEM [40] for room acoustic simulation with frequency-dependent absorbing BCs. As the main result, we can report whether or not TD-FEM can simulate acoustics in 2D real-scale room accurately at wide frequencies, and with lower computational costs than FD-FEM. The remainder of this study is organized as follows. Section 2 presents the theory of TD-FEM for room acoustic simulations with frequency-dependent absorbing boundaries. In Sec. 3, its discretization error characteristics are examined with an impedance tube problem in comparison with theory and FD-FEM. Section 4 demonstrates the TD-FEM performance benefits over FD-FEM via acoustic simulations in a 2D real-scale office and a concert hall. Section 5 concludes the discussion presented in this paper.

2. Room Acoustic Simulations with TD-FEM

This section presents a description of a room acoustic solver with implicit TD-FEM, including frequency-dependent BCs [18]. The implicit TD-FEM is based on the fourth-order accurate TD-FEM described in the literature [15]. The frequency-dependent boundary condition is incorporated with ADE method [35, 36]. It is noteworthy that the TD-FEM uses eight-node hexahedral elements for 3D analysis and four-node quadrilateral elements for 2D analysis, respectively using modified integration rules [30] for reducing dispersion error. The present study uses the 2D solver for room acoustic simulations. Although the present study uses specific elements for spatial discretization, the formulation itself can apply to any type of finite element.

2.1. Wave equation and finite element discretization in space

We consider sound wave propagation in an interior domain Ω surrounded by boundary Γ, which is described by the following acoustic wave equation as

$$\frac{\partial^2 p(\boldsymbol{r},t)}{\partial t^2} - c_0^2 \nabla^2 p(\boldsymbol{r},t) = \rho_0 c_0^2 \frac{\partial q(\boldsymbol{r},t)}{\partial t} \delta(\boldsymbol{r}-\boldsymbol{r}_\mathrm{a}), \ \text{ in } \ \Omega \tag{1}$$

where p signifies the sound pressure, c_0 denotes the speed of sound, ρ_0 stands for the air density, q expresses the volume velocity of a sound source, and δ represents the delta function. Additionally, $\boldsymbol{r}$ is the position vector of an arbitrary point in the domain; $\boldsymbol{r}_\mathrm{a}$ is the position vector of a point source. For the boundary Γ, we assume three BCs: The rigid boundary Γ_0, the vibration boundary Γ_v, and the absorbing boundary Γ_a as presented below.

$$\frac{\partial p(\boldsymbol{r},t)}{\partial n} = \begin{cases} 0 & \text{on } \Gamma_0 \\ -\rho_0 \dot{v}_\mathrm{n}(\boldsymbol{r},t) & \text{on } \Gamma_\mathrm{v} \\ -\frac{1}{c_0}\int_{-\infty}^{t} y_\mathrm{n}(\boldsymbol{r},t-\tau)\dot{p}(\boldsymbol{r},\tau)d\tau & \text{on } \Gamma_\mathrm{a} \end{cases} \tag{2}$$

In those equations, v_n represents the vibration velocity, $\cdot$ is the first-order derivative with respect to time; y_n is the specific acoustic admittance ratio in the time domain. The weak form of the wave equation for finite element discretization is

$$\begin{aligned} \int_\Omega \left[\Phi(\boldsymbol{r},t)\frac{\partial^2 p(\boldsymbol{r},t)}{\partial t^2} + c_0^2 \nabla\Phi(\boldsymbol{r},t)\nabla p(\boldsymbol{r},t) \right] d\Omega - c_0^2 \int_\Gamma \Phi(\boldsymbol{r},t)\frac{\partial p(\boldsymbol{r},t)}{\partial n} d\Gamma \\ = \rho_0 c_0^2 \frac{\partial q(\boldsymbol{r},t)}{\partial t} \int_\Omega \Phi(\boldsymbol{r},t)\delta(\boldsymbol{r}-\boldsymbol{r}_\mathrm{a}) d\Omega, \end{aligned} \tag{3}$$

where the Φ is the arbitrary weight function. We apply finite element discretizations to Eq. (1) together with the three BCs in Eq. (2). The following semi-discretized matrix equation is obtained [18]:

$$\boldsymbol{M}\ddot{\boldsymbol{p}} + c_0^2 \boldsymbol{K}\boldsymbol{p} + c_0 \boldsymbol{C}'(\check{y} * \dot{\boldsymbol{p}}) = \boldsymbol{f}. \tag{4}$$

Here, $\boldsymbol{M}$ stands for the global mass matrix, $\boldsymbol{K}$ expresses the global stiffness matrix, and $\boldsymbol{C}'$ denotes the global dissipation matrix (not including the admittance term). Vector $\boldsymbol{p}$ is the sound pressure vector. Also, $\boldsymbol{f}$ is the external force vector. The symbol $\cdot\cdot$ signifies the second-order derivative with respect to time. Details of the global matrices and the convolution in the third term are given as

$$\boldsymbol{M} = \sum_e \boldsymbol{m}_\mathrm{e} = \sum_e \int_{\Omega_\mathrm{e}} \boldsymbol{N}^T \boldsymbol{N} d\Omega_\mathrm{e}, \tag{5}$$

$$\boldsymbol{K} = \sum_e \boldsymbol{k}_\mathrm{e} = \sum_e \int_{\Omega_\mathrm{e}} \nabla\boldsymbol{N}^T \nabla\boldsymbol{N} d\Omega_\mathrm{e}, \tag{6}$$

$$\boldsymbol{C}' = \sum_e \boldsymbol{c}_{\mathrm{e}}' = \sum_e \int_{\Gamma_{\mathrm{e}}} \boldsymbol{N}^T \boldsymbol{N} d\Gamma_{\mathrm{e}}, \tag{7}$$

$$\check{y} * \dot{\boldsymbol{p}} = \int_{-\infty}^{t} y_{\mathrm{n}}(\boldsymbol{r}, t-\tau)\dot{\boldsymbol{p}}(\tau)d\tau, \tag{8}$$

where $\boldsymbol{m}_{\mathrm{e}}$, $\boldsymbol{k}_{\mathrm{e}}$, and $\boldsymbol{c}_{\mathrm{e}}'$ respectively represent the element matrices with respect to $\boldsymbol{M}$, $\boldsymbol{K}$ and $\boldsymbol{C}'$. The vector $\boldsymbol{N}$ is the shape function vector. In addition, $d\Omega_{\mathrm{e}}$ and $d\Gamma_{\mathrm{e}}$ respectively denote the domain and the boundary integrals in terms of an element.

2.2. Implementation of frequency-dependent absorbing boundary condition

In ADE method [35, 36] the frequency-domain specific acoustic admittance ratio $y_{\mathrm{n}}(\omega)$ is approximated by the rational function defined as

$$y_{\mathrm{n}}(\omega) \approx \frac{a_0 + \cdots + a_N(-j\omega)^N}{1 + \cdots + b_N(-j\omega)^N}, \tag{9}$$

where ω represents the angular frequency, j denotes the imaginary unit, a_i and b_i are the coefficients of the polynomials, and N stands for the order of the polynomials. The equation above can be described by partial fraction decomposition as

$$y_{\mathrm{n}}(\omega) \approx y_\infty + \sum_{i=1}^{n_{\mathrm{rp}}} \frac{A_i}{\lambda_i + j\omega} + \sum_{i=1}^{n_{\mathrm{cp}}} \left(\frac{B_i \pm jC_i}{\alpha_i \pm j\beta_i + j\omega} \right). \tag{10}$$

Here, y_∞, A_i, B_i, and C_i are the real-valued coefficients, n_{rp} denotes the number of real poles λ_i, and n_{cp} stands for the number of the pair of complex conjugate poles $\alpha_i \pm j\beta_i$. Inserting the inverse Fourier transformed value of Eq. (10) into Eq. (8) engenders the following equation.

$$\check{y} * \dot{\boldsymbol{p}} = y_\infty \dot{\boldsymbol{p}} + \sum_{i=1}^{n_{\mathrm{rp}}} A_i \boldsymbol{\phi}_i + 2 \sum_{i=1}^{n_{\mathrm{cp}}} [B_i \boldsymbol{\psi}_i^{(1)} + C_i \boldsymbol{\psi}_i^{(2)}]. \tag{11}$$

Here, the auxiliary functions $\boldsymbol{\phi}_i$, $\boldsymbol{\psi}_i^{(1)}$, and $\boldsymbol{\psi}_i^{(2)}$ are called accumulators. Those functions are calculated by solving the following simultaneous first-order ordinary differential equations (ODEs).

$$\dot{\boldsymbol{\phi}}_i + \lambda_i \boldsymbol{\phi}_i = \dot{\boldsymbol{p}}, \tag{12}$$

$$\dot{\boldsymbol{\psi}}_i^{(1)} + \alpha_i \boldsymbol{\psi}_i^{(1)} + \beta_i \boldsymbol{\psi}_i^{(2)} = \dot{\boldsymbol{p}}, \tag{13}$$

$$\dot{\boldsymbol{\psi}}_i^{(2)} + \alpha_i \boldsymbol{\psi}_i^{(2)} - \beta_i \boldsymbol{\psi}_i^{(1)} = \boldsymbol{0}. \tag{14}$$

We solve the ODEs above using Crank–Nicolson method. Substituting Eq. (11) into Eq. (4) engenders a semi-discretized equation considering frequency-dependent absorbing BCs incorporated by the ADE method as

$$\boldsymbol{M}\ddot{\boldsymbol{p}} + c_0^2 \boldsymbol{K}\boldsymbol{p} + c_0 y_\infty \boldsymbol{C}' \dot{\boldsymbol{p}} = \boldsymbol{f} - c_0 \boldsymbol{C}' \left[\sum_{i=1}^{n_{\mathrm{rp}}} A_i \boldsymbol{\phi}_i + 2 \sum_{i=1}^{n_{\mathrm{cp}}} (B_i \boldsymbol{\psi}_i^{(1)} + C_i \boldsymbol{\psi}_i^{(2)}) \right]. \tag{15}$$

2.3. Time discretization using Fox–Goodwin method

For time discretization, we use the conditionally stable Fox–Goodwin method, a family of Newmark β method [31, 32], as a direct time integration method. The resulting time-marching scheme is given as

$$(\boldsymbol{M} + \beta c_0^2 \Delta t^2 \boldsymbol{K} + \frac{c_0 \Delta t y_\infty}{2} \boldsymbol{C}') \ddot{\boldsymbol{p}}^{n+1} = \boldsymbol{f}^{n+1} - c_0^2 \boldsymbol{K} \boldsymbol{P}_1 - c_0 \boldsymbol{C}' (y_\infty \boldsymbol{P}_2 + \boldsymbol{P}_3), \tag{16}$$

$$\boldsymbol{p}^{n+1} = \boldsymbol{p}^n + \Delta t \dot{\boldsymbol{p}}^n + \Delta t^2 (\frac{1}{2} - \beta) \ddot{\boldsymbol{p}}^n + \Delta t^2 \beta \ddot{\boldsymbol{p}}^{n+1}, \tag{17}$$

$$\dot{\boldsymbol{p}}^{n+1} = \dot{\boldsymbol{p}}^n + \frac{\Delta t}{2} (\ddot{\boldsymbol{p}}^n + \ddot{\boldsymbol{p}}^{n+1}), \tag{18}$$

with

$$\boldsymbol{P}_1 = \boldsymbol{p}^n + \Delta t \dot{\boldsymbol{p}}^n + \Delta t^2 (\frac{1}{2} - \beta) \ddot{\boldsymbol{p}}^n, \quad \boldsymbol{P}_2 = \dot{\boldsymbol{p}}^n + \frac{\Delta t}{2} \ddot{\boldsymbol{p}}^n, \tag{19}$$

$$\boldsymbol{P}_3 = \sum_{i=1}^{n_{\mathrm{rp}}} A_i \boldsymbol{\phi}_i^{n+1} + 2 \sum_{i=1}^{n_{\mathrm{cp}}} (B_i \boldsymbol{\psi}_i^{(1),n+1} + C_i \boldsymbol{\psi}_i^{(2),n+1}). \tag{20}$$

Here, Δt represents the time interval between time step n and $n+1$. In addition, β is a parameter for Newmark β method, which is set as $\beta = 1/12$ for Fox–Goodwin method. With Crank-Nicolson method, the ODEs related to the accumulators are solvable as

$$\begin{aligned} \boldsymbol{\phi}_i^{n+1} &= \frac{\Delta t}{D_1} \dot{\boldsymbol{p}}^{n+1} + \boldsymbol{X}_1 \\ \boldsymbol{X}_1 &= \frac{(2 - \lambda_i \Delta t) \boldsymbol{\phi}_i^n + \Delta t \dot{\boldsymbol{p}}^n}{D_1} \\ D_1 &= 2 + \lambda_i \Delta t, \end{aligned} \tag{21}$$

$$\boldsymbol{\psi}_i^{(1),n+1} = \frac{2\Delta t + \alpha_i \Delta t^2}{D_2} \dot{\boldsymbol{p}}^{n+1} + \boldsymbol{X}_2$$
$$\boldsymbol{X}_2 = \frac{[4 - (\alpha_i^2 + \beta_i^2)\Delta t^2]\boldsymbol{\psi}_i^{(1),n} + (2\Delta t + \alpha_i \Delta t^2)\dot{\boldsymbol{p}}^n - 4\beta_i \Delta t \boldsymbol{\psi}_i^{(2),n}}{D_2}$$
$$D_2 = 4 + 4\alpha_i \Delta t + (\alpha_i^2 + \beta_i^2)\Delta t^2, \tag{22}$$

$$\boldsymbol{\psi}_i^{(2),n+1} = \frac{\beta_i \Delta t^2}{D_2} \dot{\boldsymbol{p}}^{n+1} + \boldsymbol{X}_3$$
$$\boldsymbol{X}_3 = \frac{[4 - (\alpha_i^2 + \beta_i^2)\Delta t^2]\boldsymbol{\psi}_i^{(2),n} + 4\beta_i \Delta t \boldsymbol{\psi}_i^{(1),n} + \beta_i \Delta t^2 \dot{\boldsymbol{p}}^n}{D_2}, \tag{23}$$

It is noteworthy that $y_\infty = y_\mathrm{n}^\mathrm{r}$ and $\boldsymbol{P}_3 = 0$ are used in Eq. (16) when using frequency-independent absorbing BCs with real valued specific admittance ratio y_n^r. Furthermore, the linear system of equations Eq. (16), which is a real symmetric matrix, is solved at each time step using an iterative solver, Conjugate Gradient (CG) method, with a diagonal scaling preconditioning [33]. The convergence tolerance is set to 10^{-6}. The matrices in Eq. (16) are stored by sparse matrix storage formats [41], such as the compressed row storage format to reduce the solver memory requirement.

2.4. Stability condition

We use the following stability condition [15], which is derived for acoustic simulation with a frequency-independent BC, for all numerical experiments performed in this study.

$$\Delta t \leq \min\left[\frac{1}{\omega_i \sqrt{0.25 - \beta}}\right]. \tag{24}$$

Here, the natural frequency ω_i is calculated by solving a generalized eigenvalue problem $[\boldsymbol{k}_{\mathrm{e},i} - (\frac{\omega_i}{c_0})^2 \boldsymbol{m}_{\mathrm{e},i}]\boldsymbol{p}_{\mathrm{e},i} = 0$ for all elements $\Omega_{\mathrm{e},i} (i = 1, ..., n_\mathrm{e})$, where $\boldsymbol{p}_\mathrm{e}$ is the sound pressure vector in an element and n_e is the element number. For Fox–Goodwin method with rectangular elements of size $d_{x,i} \times d_{y,i}$ where $d_{x,i}$ and $d_{y,i}$ respectively denote the i-th element length in x and y directions, the stability condition can be written simply as

$$\Delta t \leq \min\left[\frac{1}{c_0 \sqrt{\frac{1}{d_{x,i}^2} + \frac{1}{d_{y,i}^2}}}\right]. \tag{25}$$

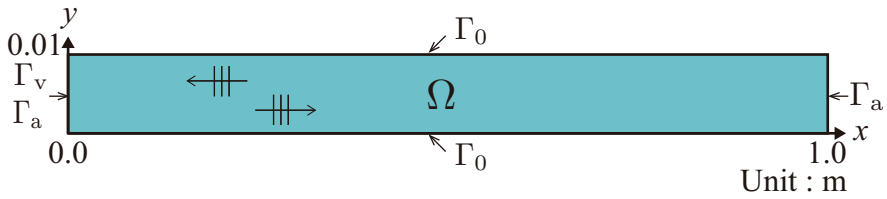

Figure 1: Impedance tube problem including frequency-dependent absorbing BCs at the tube end.

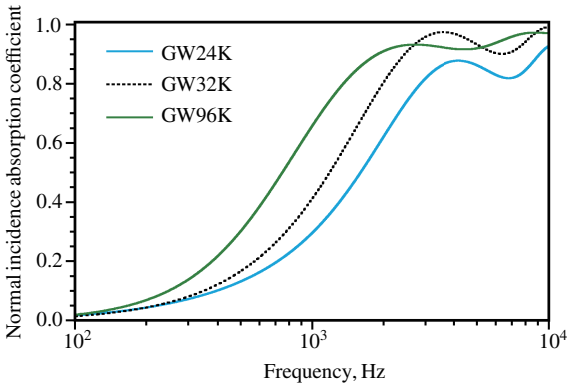

Figure 2: Normal incidence sound absorption coefficient of three GW absorbers.

Furthermore, for square elements, the stability condition is defined as $\Delta t \leq \frac{h}{\sqrt{2}c_0}$ with element length h. For more detailed information including the stability condition for 3D analysis, an earlier report [15] is available. The present time-marching scheme must solve additional ODEs in Eqs. (12)–(14) using the Crank–Nicolson method. Therefore the stability condition might change from Eq. (24). However, we confirmed that Eq. (24) is valid for all the numerical experiments in this work.

3. Discretization Error Characteristics

This section presents the discretization error characteristics of the implicit TD-FEM using the impedance tube problem, as shown in Fig. 1. The impedance tube has a frequency-dependent absorbing boundary Γ_a at the tube end, where specific acoustic admittance ratio of a porous absorbing material, glass wool (GW), is imposed. Three GWs with different flow resistivity are considered. The tube inlet has vibration boundary Γ_v, where the absorbing boundary with specific acoustic admittance of the air is also

imposed. Other boundaries are rigid. The reflection coefficient at the absorbing surface is calculated with the implicit TD-FEM according to the transfer function method [42] using two microphones. The results are compared with theoretical results obtained using the transfer matrix method [43]. The implicit TD-FEM results are also compared with results obtained from fourth-order accurate FD-FEM using the modified integration rule [40, 44]. We used a 2D version of the FD-FEM using four-node quadrilateral elements. The implicit TD-FEM and the FD-FEM use the same dispersion-reduced finite elements for spatial discretization, meaning that both methods have an equal magnitude of spatial discretization error. The speed of sound and the density of air are set respectively as 343.7 m/s and 1.205 kg/m^2 throughout the numerical experiments performed in the present paper.

3.1. Setup of FE analysis

We considered three spatial resolution meshes to show the convergence rate of the solution. The three meshes, Mesh 1 - Mesh 3, were created with square elements having different lengths h: 0.005 m for Mesh 1, 0.0025 m for Mesh 2, and 0.00125 m for Mesh 3. Spatial resolutions for Mesh 1–Mesh 3 respectively show 6.9, 13.7 and 27.5 elements per wavelength at the upper-limit frequency of 10 kHz. For the respective meshes, we set four time intervals to elucidate the effects of time discretization error. The four time intervals are $\Delta t = \Delta t_{\mathrm{crit}}$, $0.5\Delta t_{\mathrm{crit}}$, $0.25\Delta t_{\mathrm{crit}}$, and $0.125\Delta t_{\mathrm{crit}}$, where Δt_{crit} represents the time interval at stability limit. A modulated Gaussian pulse was given to the vibration boundary at the tube inlet with the upper-limit frequency of 10 kHz. Two receivers were placed at (x, y)=(0.94, 0.005) and (0.95, 0.005). From the sound pressure at the two receivers, we calculated the reflection coefficient according to the transfer function method [42]. The time response was calculated up to 1 s. However, for FD-FEM, frequency responses were computed at frequencies of 100 Hz to 10 kHz with 1 Hz interval. At the tube end, we gave specific acoustic admittance ratio of rigidly backed GW absorber with different flow resistivity R: GW24K, R=6,900 Pa s/m^2; GW32K, R=13,900 Pa s/m^2; and GW96K, R=55,000 Pa s/m^2. The absorber thickness is 25 mm. We used the Miki model [45] to describe the fluid properties of GW, i.e., the characteristic impedance and the complex wavenumber. As a reference, Figure 2 presents normal incidence sound absorption coefficient of three GW absorbers.

For the ADE method, the three specific acoustic admittance ratios $y_{\mathrm{n}}(\omega)$ of rigidly backed GW absorbers using the transfer matrix method were ap-

proximated at frequencies of 100 Hz to 10 kHz with the rational function form of Eq. (10). The parameters y_∞, A_i, B_i, C_i, λ_i, α_i, and β_i were obtained using the vector-fitting method [46]. The quantities of real poles and pairs of complex conjugate poles were $n_{\mathrm{rp}} = 4$, $n_{\mathrm{cp}} = 3$ for GW24K, $n_{\mathrm{rp}} = 3$, $n_{\mathrm{cp}} = 3$, respectively, for GW32K, and $n_{\mathrm{rp}} = 8$, $n_{\mathrm{cp}} = 3$ for GW96K. We gave the fitted parameters in Appendix A.

3.2. Accuracy measure

To evaluate the accuracy of the implicit TD-FEM, we defined the relative error norm from theoretical values with respect to the magnitude and phase of the reflection coefficient r.

$$\|\varepsilon_{\mathrm{amp}}\|_2 = \frac{\sqrt{\sum_{i=1}^{n_{\mathrm{f}}} |\tilde{r}_{\mathrm{amp}}(\omega_i) - r_{\mathrm{amp}}(\omega_i)|^2}}{\sqrt{\sum_{i=1}^{n_{\mathrm{f}}} |r_{\mathrm{amp}}(\omega_i)|^2}}, \tag{26}$$

$$\|\varepsilon_{\theta}\|_2 = \frac{\sqrt{\sum_{i=1}^{n_{\mathrm{f}}} |\tilde{r}_{\theta}(\omega_i) - r_{\theta}(\omega_i)|^2}}{\sqrt{\sum_{i=1}^{n_{\mathrm{f}}} |r_{\theta}(\omega_i)|^2}}. \tag{27}$$

Therein, $\tilde{r}_{\mathrm{amp}}(\omega_i)$ and $\tilde{r}_{\theta}(\omega_i)$ respectively represent the amplitude and phase of r calculated using FEM. In addition, $r_{\mathrm{amp}}(\omega_i)$ and $r_{\theta}(\omega_i)$ respectively represent the corresponding theoretical values calculated using the transfer matrix method. Additionally, n_{f} is the number of frequencies.

3.3. Results and discussion

Figures 3(a) and 3(b), respectively show a comparison of reflection coefficients r calculated using TD-FEM with the four Δts, theory, and FD-FEM for the case of GW96K using Mesh 1. It is noteworthy that the presented figures show the highest error case using the coarsest mesh. We selected this case because of the ease of understanding the error behaviors of the two methods. The left and right panels respectively portray the amplitude and phase of r. The lower panel shows their enlarged view above 6 kHz. Results show that TD-FEM is the most accurate at the stability limit for both the amplitude and phase of r. The discrepancies calculated based on theory are larger for smaller Δt; the TD-FEM results finally converge to FD-FEM results. As demonstrated later, the error behavior depends on the flow resistivity R of GW. For GW24K and GW32K having lower R, the amplitude of r by TD-FEM shows a better fit to theory at the stability limit, but the discrepancy becomes large for smaller Δt. For the phase of r in terms of

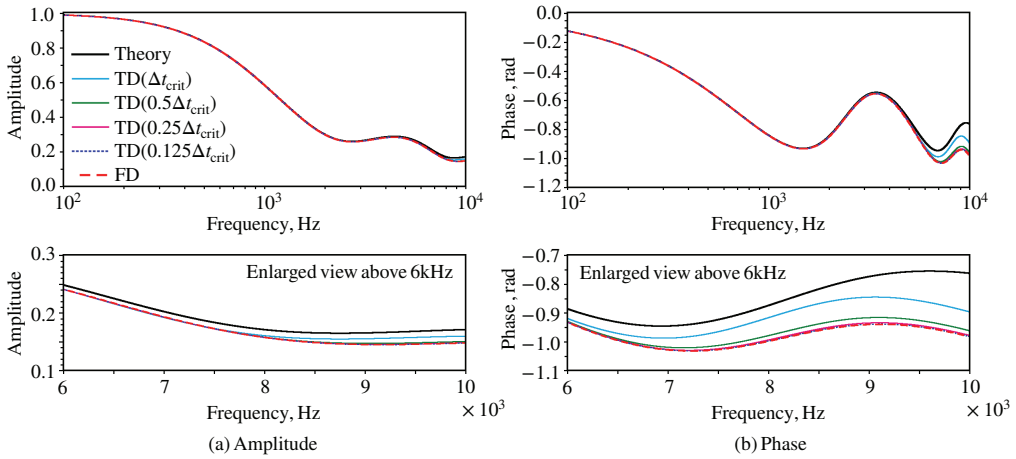

Figure 3: Reflection coefficient r of GW96K calculated using implicit TD-FEM (TD) with four Δt, theory, and FD-FEM (FD): (a) amplitude of r and (b) phase of r; the lower panels show the enlarged view above 6 kHz. The coarsest Mesh 1 is used in FEM analysis.

GW24K and GW32K, the TD-FEM shows an enormous discrepancy from theory at the stability limit, but the discrepancy decreases for smaller Δt. The TD-FEM results for GW24K and GW32K also converge to FD-FEM results for sufficiently small Δt. That convergence to FD-FEM results is explainable by the respective theoretical dispersion error characteristics in an idealized case. In earlier works [15, 30, 40, 44], which present theoretical dispersion error equations calculated using dispersion error analysis, the magnitude of dispersion errors of the TD-FEM and FD-FEM becomes the same in the limit $\Delta t \to 0$. In two dimensions, the theoretically estimated dispersion errors $e_{\mathrm{dis,TD}}$ for the TD-FEM, and $e_{\mathrm{dis,FD}}$ for the FD-FEM are described respectively as

$$e_{\mathrm{dis,TD}} \approx \frac{k^4}{480}[d_x^4 \cos^6\theta + d_y^4 \sin^6\theta - (c_0\Delta t)^4] \text{ and} \tag{28}$$

$$e_{\mathrm{dis,FD}} \approx \frac{k^4}{480}[d_x^4 \cos^6\theta + d_y^4 \sin^6\theta], \tag{29}$$

where k is the wavenumber and where θ is the propagation direction of plane wave in two-dimensional polar coordinates system. In addition, the dispersion equations show that TD-FEM has a better accuracy than FD-FEM at the stability limit. Although the theoretical estimation assumes plane wave propagation in a free field, in the qualitative sense, it is apparently valid for

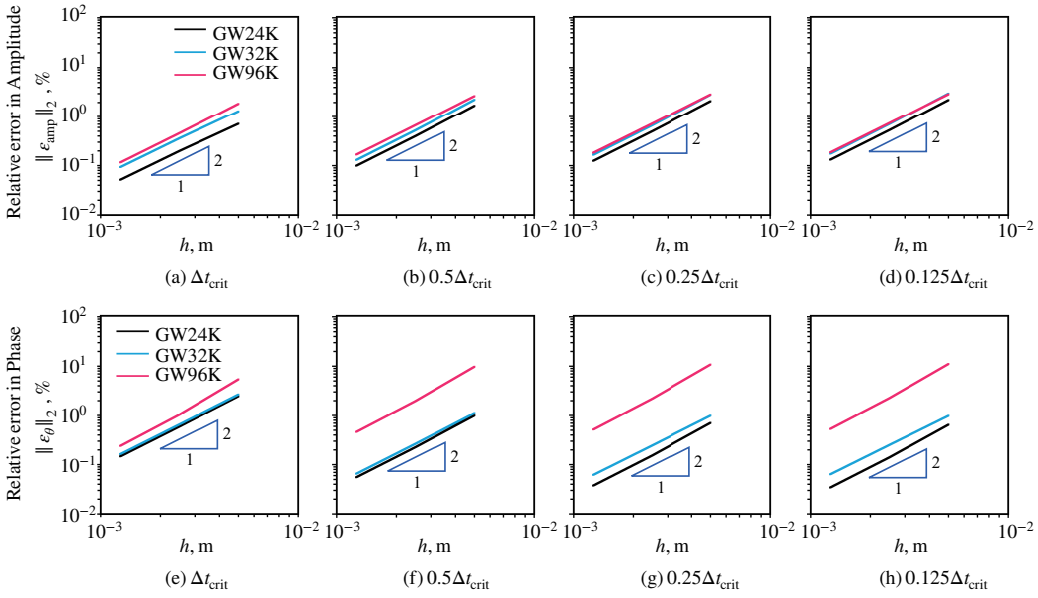

Figure 4: Convergence of relative error norm $\|\varepsilon_{\text{amp}}\|_2$ and $\|\varepsilon_{\theta}\|_2$ in terms of element length h at each Δt: (Upper) Amplitude (a) Δt_{crit}, (b) $0.5\Delta t_{\text{crit}}$, (c) $0.25\Delta t_{\text{crit}}$, and (d) $0.125\Delta t_{\text{crit}}$; and (Lower) Phase (e) Δt_{crit}, (f) $0.5\Delta t_{\text{crit}}$, (g) $0.25\Delta t_{\text{crit}}$, and (h) $0.125\Delta t_{\text{crit}}$.

the numerical results presented here, considering the frequency-dependent absorbing BC. We show that the convergence still holds for more practical conditions, as described in the next section.

As quantitative evaluations in the error magnitude of the TD-FEM, Figures 4(a)–(h) show convergence of the relative error norm $\|\varepsilon_{\text{amp}}\|_2$ and $\|\varepsilon_{\theta}\|_2$ in terms of element length h at each Δt. In terms of both the amplitude and phase of r, the error magnitude depends on R of GW: it becomes smaller for lower R at all Δt. It is noteworthy that the error behavior, i.e., smaller error for lower R of GW, is the same for FD-FEM analysis in air-porous coupled problems where the porous-domain modeled with an equivalent fluid absorption elements as an extended-reaction model [47]. The possible reason for the error increase is attributable to the number of elements per wavelength becoming smaller because of the slower sound speed in porous materials with higher R. Furthermore, the convergence rates in $\|\varepsilon_{\text{amp}}\|_2$ and $\|\varepsilon_{\theta}\|_2$ approximate to 2 in all cases. As shown in Fig. 5(a) and 5(b), this convergence rate is the same as the FD-FEM. The error magnitude of the TD-FEM and the FD-FEM becomes equal for smaller Δt values. Furthermore, the TD-FEM

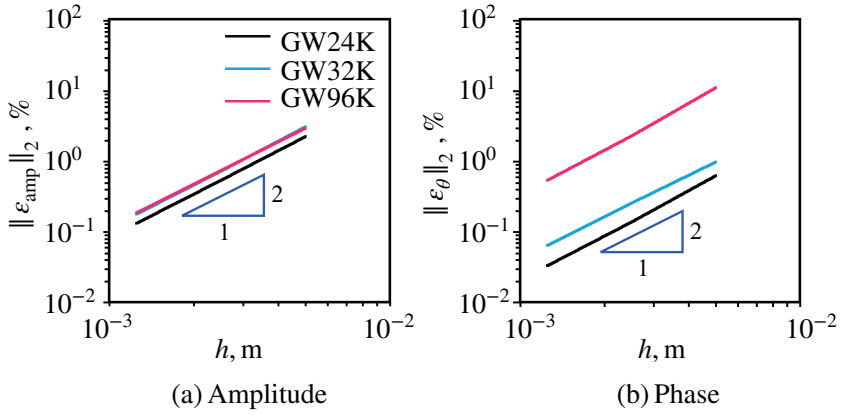

Figure 5: Convergence of relative error norm $\|\varepsilon_{\text{amp}}\|_2$ and $\|\varepsilon_\theta\|_2$ in terms of element length h for FD-FEM: (a) amplitude and (b) phase.

and FD-FEM errors are lower for the meshes having higher spatial resolution, meaning that the results of both methods finally converge to the theoretical values. Numerical results indicate that the implicit TD-FEM with the frequency-dependent absorbing BCs can perform acoustic simulations having a similar level of accuracy as the FD-FEM with the same convergence rate. Although TD-FEM has fourth-order accuracy for an idealized condition, i.e., the plane wave propagation in a free field, the numerical results also revealed that the convergence rate is reduced to second-order for the case with frequency-dependent impedance boundaries. It is probably attributable to dispersion minimization, not working well for elements on impedance boundaries. Its improvement is left as a subject for future study.

4. Performance Comparison in Real-scale 2D Room Acoustic Problems

This section presents the implicit TD-FEM performance compared to the FD-FEM via real-scale 2D room acoustic problems, including frequency-dependent absorbing BCs. Comparison was made in both frequency and time domains. First, we show a performance comparison in an office model (39.92 m^2 area) discretized with uniform-sized square elements. Then, the implicit TD-FEM performance is demonstrated using a larger and more complicated concert hall model (296 m^2 area) discretized by variously sized irregular shaped elements. Both models were used in earlier studies [17, 48],

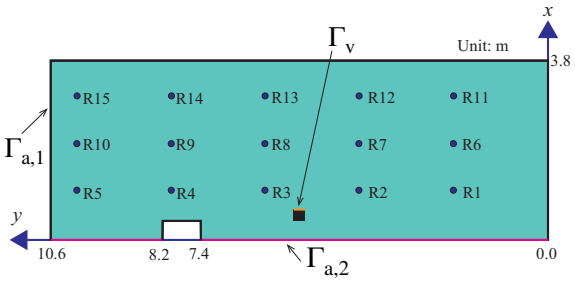

Reciever location, (x, y)	
R1 (1.0, 2.0)	R9 (2.0, 8.0)
R2 (1.0, 4.0)	R10 (2.0, 10.0)
R3 (1.0, 6.0)	R11 (3.0, 2.0)
R4 (1.0, 8.0)	R12 (3.0, 4.0)
R5 (1.0, 10.0)	R13 (3.0, 6.0)
R6 (2.0, 2.0)	R14 (3.0, 8.0)
R7 (2.0, 4.0)	R15 (3.0, 10.0)
R8 (2.0, 6.0)	

Figure 6: Office model.

for which different boundary conditions were assumed to examine the performance of other wave-based room acoustic solvers. For frequency-dependent absorbing BCs in both office and hall models, we assumed the same three absorption characteristics of GW, i.e., GW24K, GW32K, and GW96K, used in an earlier section. The rational function form in ADE method is also identical. Additionally, we applied a highly efficient sparse direct solver, PARDISO (included in Intel Math Kernel Library), with the FD-FEM for solving the linear system of equations at each frequency. Because the coefficient matrix of FD-FEM becomes complex symmetric matrix, we selected "complex and structurally symmetric" matrix type in the PARDISO setup. All computations were performed using a computer (Mac Pro 2020; Apple Inc., Xeon CPU W 2.7 GHz, 24 cores; Intel Corp.) with a Fortran compiler (ver. 2020; Intel Corp.). We used the sparse direct solver to the FD-FEM instead of iterative solvers because a preliminary test, as shown in Appendix B, showed higher efficiency of using the sparse direct solver than an iterative solver, CSQMOR method [49] with diagonal scaling, which was an efficient solver for solving real sized 3D room acoustics problems in the authors' earlier work [40] where performance of the four iterative solvers, COCG [50], COCR [51], CSQMR [52], and CSQMOR, for complex-symmetric matrices were examined.

4.1. Office model

4.1.1. Problem description and numerical setup

Figure 6 presents the office model. We calculated sound fields generated by sound radiation from a loudspeaker, which is treated by the vibration boundary Γ_{v}. The room's boundary has a weakly absorbing frequency-independent boundary $\Gamma_{\mathrm{a},1}$ and frequency-dependent absorbing boundary

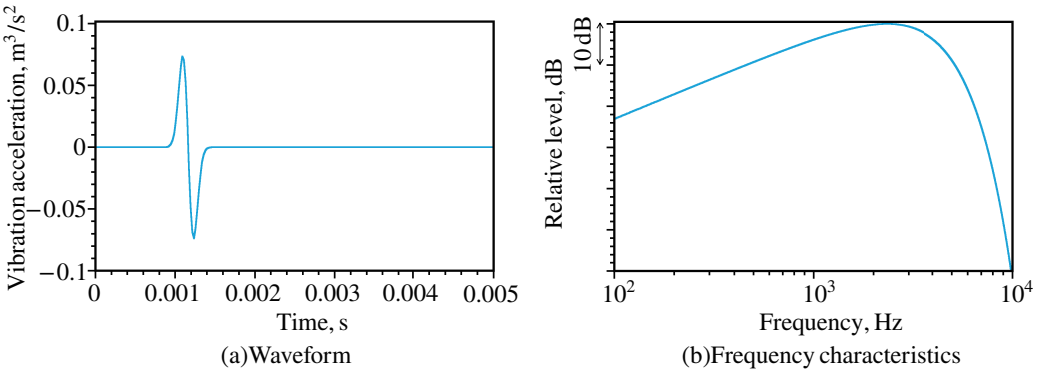

Figure 7: Sound source for office problem: (a) waveform and (b) frequency characteristics.

$\Gamma_{a,2}$. $\Gamma_{a,1}$ has a real-valued specific acoustic admittance ratio $y_n^r = 1/37.97$ corresponding to the normal incidence sound absorption coefficient α_0 of 0.1. For $\Gamma_{a,2}$, we assumed the three absorbing conditions for which the specific acoustic admittance ratios of GW24K, GW32K, and GW96K were given, respectively. Receiving points were placed at 15 positions: R1–R15. The upper-limit frequency was assumed as 4.5 kHz.

Regarding spatial discretization, the domain was discretized with square elements of 0.01 m length. The resulting mesh has 400,720 DOF. The spatial resolution is 7.6 elements per wavelength at the upper-limit frequency of 4.5 kHz. As an initial condition of TD-FEM, we gave the modulated Gaussian pulse waveform having frequency characteristics in Fig. 7 to the vibration boundary. Source function $s(t)$ is given as [15]

$$s(t) = \frac{2\pi}{\rho_0}(0.4 - c_0 t)e^{\frac{-(0.4-c_0 t)^2}{d^2}}, \tag{30}$$

where π is the circular constant, and the parameter d is defined as $d = \frac{c_0 e}{2\pi f_{\max}}$ with the upper-limit frequency $f_{\max}$. The TD-FEM calculation was performed up to 1 s with the two time intervals $\Delta t = \Delta t_{\text{crit}}$ and $0.25\Delta t_{\text{crit}}$ to show convergence to FD-FEM results. The stability limit is Δt_{crit}=1/48,607 s. However, for FD-FEM calculations, vibration acceleration of 1 m^3/s^2 was given to the vibration boundary. The analyzed frequency range is 100 Hz to 4.5 kHz with a 1 Hz interval.

4.1.2. Measure of accuracy

Two accuracy measures were defined from practical points of view in room acoustic applications. First, to evaluate the differences in frequency re-

sponses calculated using the TD-FEM and FD-FEM, we defined the following absolute difference in terms of sound pressure level (SPL) distributions.

$$D_{\mathrm{abs}}(f_{\mathrm{m}}) = \frac{1}{N_{\mathrm{p}}} \sum_{i=1}^{N_{\mathrm{p}}} |L_{\mathrm{f}}(f_{\mathrm{m}}, \boldsymbol{r}_i) - L_{\mathrm{t}}(f_{\mathrm{m}}, \boldsymbol{r}_i)|. \tag{31}$$

In that equation, $L_{\mathrm{f}}(f_{\mathrm{m}}, \boldsymbol{r}_i)$ and $L_{\mathrm{t}}(f_{\mathrm{m}}, \boldsymbol{r}_i)$ respectively denote the $1/N$ octave band SPL at center frequency f_{m} calculated using the FD-FEM and TD-FEM. In addition, N_{p} stands for the number of receiving points. Here, we set $N = 3$ and 192, i.e., $D_{\mathrm{abs}}(f_{\mathrm{m}})$ was evaluated by 1/3 and 1/192 octave band SPLs. We used the 1/192 octave band SPL to permit a slight shift of frequency at which peaks and dips occur at high frequencies because of the dispersion error. However, the evaluation is still strict because the bandwidth is only 16 Hz at the highest 4491 Hz.

Another accuracy measure was defined in the time domain to quantify the similarity of two waveforms calculated using the TD-FEM and FD-FEM. We quantified the similarity with cross-correlation coefficient CC defined below as

$$CC = \frac{\sum_{n=1}^{N_{\mathrm{step}}} p_f^n p_t^n}{\sqrt{\sum_{n=1}^{N_{\mathrm{step}}} (p_f^n)^2} \sqrt{\sum_{n=1}^{N_{\mathrm{step}}} (p_t^n)^2}}, \tag{32}$$

where p_f^n and p_t^n respectively denote the sound pressure at time step n calculated using FD-FEM and TD-FEM. For FD-FEM, the time-domain sound pressure was calculated using the inverse Fourier transform of frequency response. In addition, N_{step} is the number of time steps.

4.2. Results and Discussion

We present a comparison of sound propagation in the office at time steps n= 500, 1,250, and 2,500, as calculated using TD-FEM for the two wall absorption cases in Figure 8. It is apparent that sound waves attenuate more for the absorption wall $\Gamma_{\mathrm{a},2}$ with GW96K at n= 1,250 and 2,500, by the higher sound absorption capability, as Figure 2 shows. Figure 9 presents a comparison of SPLs at a receiver R1 calculated using FD-FEM and TD-FEM with Δt_{crit} in the case with GW24K. The TD-FEM result is the transfer function value removing the sound source characteristics, i.e., the following calculation was made as

$$\mathrm{SPL}(\boldsymbol{r}, \omega) = 20 \log_{10} \frac{\left| \frac{p_t(\boldsymbol{r}, \omega)}{p_s(\omega)} \right|}{\sqrt{2} p_0} \ [\mathrm{dB}], \tag{33}$$

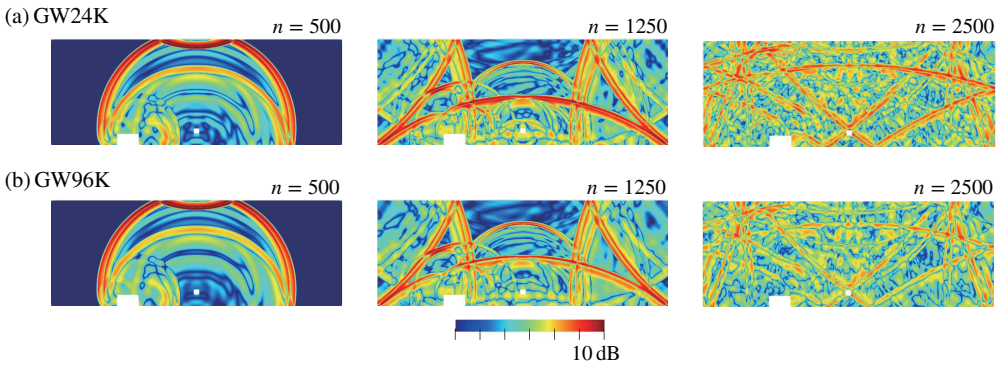

Figure 8: Comparison of SPL distributions in the office at 500, 1250, and 2500 time steps for different wall absorption settings calculated using TD-FEM: (a) GW24K and (b) GW96K.

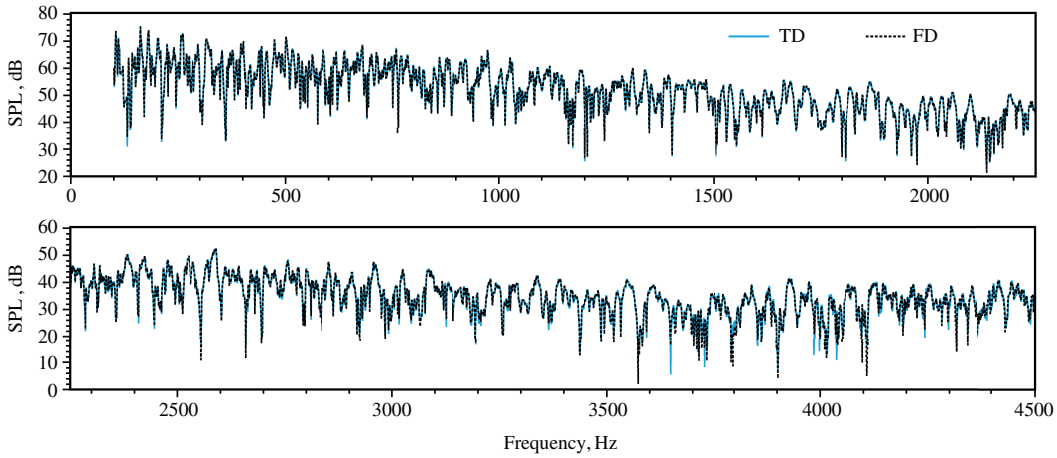

Figure 9: Comparison of SPLs at R1 calculated using FD-FEM (FD) and TD-FEM (TD) at stability limit for the case with GW24K.

where $p_t(\boldsymbol{r}, \omega)$ and $p_s(\omega)$ are, respectively, the Fourier transformed values of the time responses by TD-FEM and the source function. In addition, p_0 is the referenced value of 20 μPa. Overall, the agreement of the two frequency responses is good at all frequencies, but slight discrepancies are observed at dips. Figures 10(a) and 10(b) show an SPL comparison at R1 between FD-FEM and TD-FEM with the two time intervals (a)Δt_{crit} and (b)$0.25\Delta t_{\text{crit}}$, which is enlarged at frequencies of 4.2–4.5 kHz. The result illustrates clearly that the TD-FEM results converge to the FD-FEM result

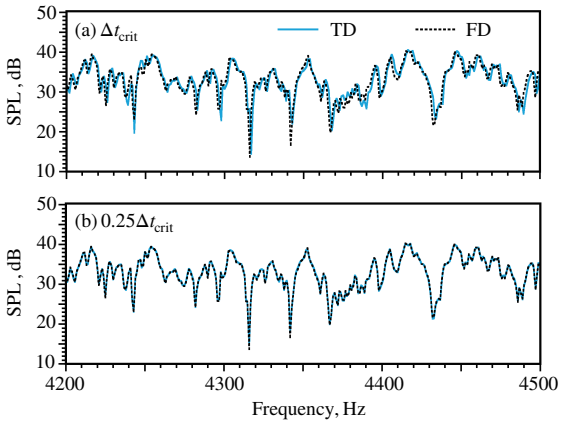

Figure 10: SPL comparison of R1 between FD-FEM (FD) and TD-FEM (TD) with (a) Δt_{crit} and (b) $0.25\Delta t_{\mathrm{crit}}$. The figures are enlarged at frequencies of 4.2–4.5 kHz.

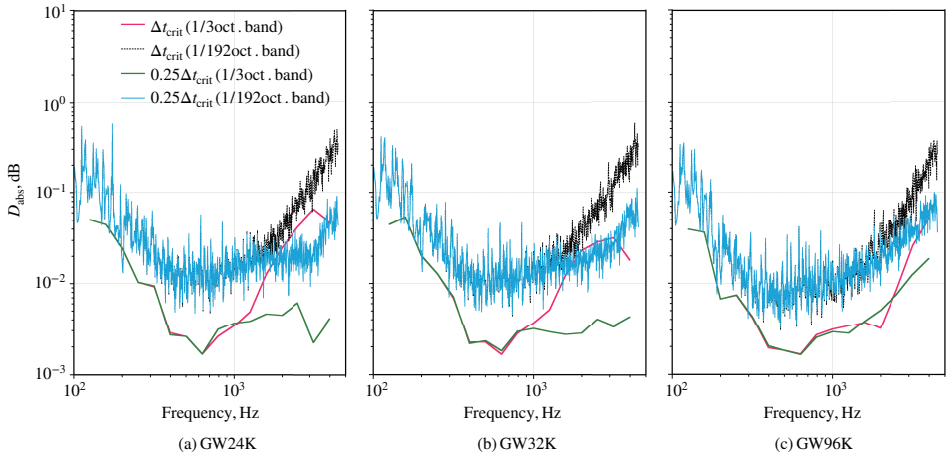

Figure 11: Absolute difference in 1/3 octave band SPL and 1/192 octave band SPL at $\Delta t = \Delta t_{\mathrm{crit}}$ and $0.25\Delta t_{\mathrm{crit}}$ for (a) GW24K, (b) GW32K, and (c) GW96K.

for a smaller time interval of $0.25\Delta t_{\mathrm{crit}}$. This point was also demonstrated by the impedance tube results presented earlier. As a reference, the frequency difference at which peaks and dips occur is only 1 Hz between the TD-FEM at the stability limit and the FD-FEM, showing that the two simulations agree well. Those results are true for all receiving points and for the cases with GW32K and GW96K.

For quantitative evaluations, Figs. 11(a)–(c) present the absolute differ-

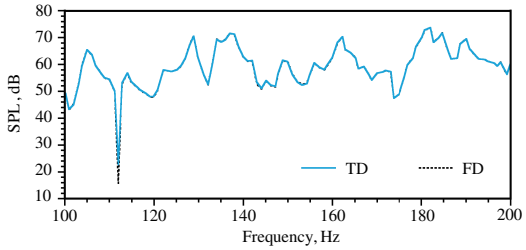

Figure 12: Comparison of SPL at R5 in frequencies of 100–200 Hz calculated using FD-FEM and TD-FEM at the stability limit for the case with GW24K. A large difference is apparent at 112 Hz.

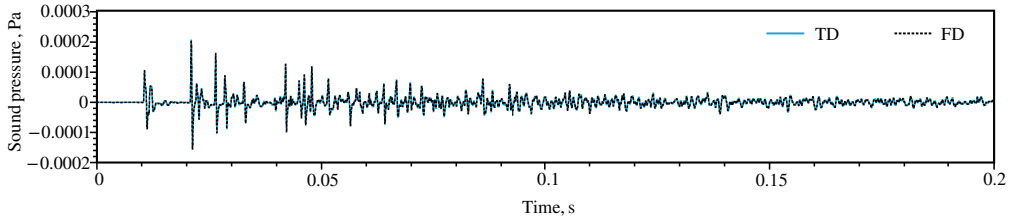

Figure 13: Comparison of time responses at R1 for the case with GW24K calculated using FD-FEM and TD-FEM with $\Delta t = \Delta t_{\mathrm{crit}}$.

ence D_{abs} in 1/3 octave band SPL and 1/192 octave band SPL at $\Delta t = \Delta t_{\mathrm{crit}}$ and $0.25\Delta t_{\mathrm{crit}}$ for the cases with (a) GW24K, (b) GW32K, and (c) GW96K. Although the D_{abs} in 1/192 octave band SPL shows large differences at some frequencies below 200 Hz for all GW cases, the values become less than 1 dB at all frequencies. Figure 12 presents an SPL comparison at R5 at frequencies below 200 Hz, showing the cause of the large difference. The difference apparently occurs at dips of SPL, which is true also for other receivers and GW cases. The number of frequencies included in a band becomes one at a frequency below 200 Hz. Therefore, large D_{abs} occurs for the evaluation in such a narrow band SPL. However, we neglect the large difference at dips from practical aspects because for more practical 1/3 octave band SPL, the D_{abs} is less than 0.1 dB at all frequencies and cases. We can find similar discussion in the literature [53, 54] where the accuracy of the phased geometrical acoustics methods was discussed. Furthermore, it is noteworthy that the large difference at dips might derive from the difference of used linear system solvers in FD-FEM and TD-FEM. Earlier work [38] showed that the difference of SPL calculated using a direct solver and an iterative

solver appears at dips in SPL. As Figure 11 shows, D_{abs} becomes smaller at frequencies higher than 1 kHz when using $0.25\Delta t_{\mathrm{crit}}$ for all GW cases.

Figure 13 presents a comparison of time responses up to 0.2 s at R1 for the case with GW24K calculated using FD-FEM and TD-FEM with $\Delta t = \Delta t_{\mathrm{crit}}$. It is noteworthy that the frequency characteristics of Gaussian pulse were considered in the FD-FEM result for comparison. Subsequently, we re-calculated the frequency response at frequencies of 1 Hz to 9 kHz with 1 Hz interval to guarantee spectrum continuity in the inverse Fourier transform. Overall, the fine structure of time responses calculated using both methods agrees excellently. This agreement can be found for all receiving point results and the other GW cases. The CC value averaged at all receiving points results exceeds 0.999 and exhibits high similarity of both waveforms.

Regarding the computational costs of the respective methods, the computational times of the TD-FEM in serial computation are 1,880–1,966 s. The computational times are 6.7–7.0 times shorter than the 13,203 s for the FD-FEM calculation at frequencies of 100 Hz to 4.5 kHz. The slight differences in the computational times of TD-FEM derive from the slight change of the convergence characteristics of the CG method for different GW cases. Particularly, the CG solver converges rapidly for the linear system solution at each time step with the mean iteration number of 5.2–5.3 per time step. The rapid convergence shows the same trend as that for the case using frequency-independent absorbing BCs [3, 15] because the coefficient matrix structure in the linear system of equations of TD-FEM with frequency-dependent absorbing BC becomes the same as that in the case using frequency-independent absorbing BCs. Furthermore, TD-FEM uses much less memory than FD-FEM does. The memory requirement of TD-FEM is 109 MBytes, which is a 1/8 smaller value than 903 MBytes of FD-FEM. It can be said that the TD-FEM can calculate a time response including broad frequency components having equal accuracy with much lower computational costs than those imposed by FD-FEM.

4.3. Concert hall model

4.3.1. Problem description and numerical setup

Figure 14 portrays the concert model, where a point source S is placed at a position $(x, y) = (22, 3.2)$ above the stage. We calculated acoustic fields generated by sound radiation from the point source, respectively using TD-FEM and FD-FEM. Sound receivers R1–R15 were placed uniformly at 15

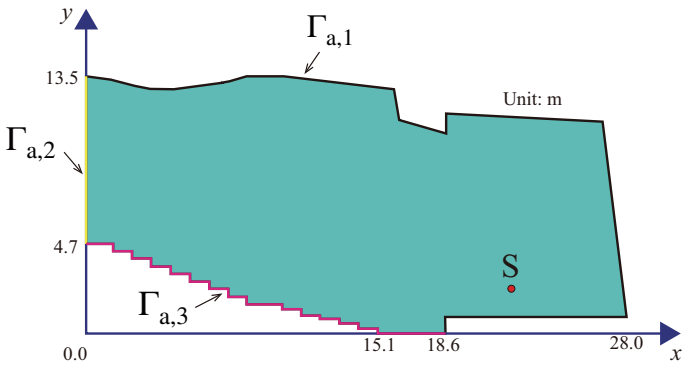

Reciever location, (x, y)			
R1	(15.1, 1.25)	R9	(6.3, 3.5)
R2	(14.1, 1.5)	R10	(5.3, 3.9)
R3	(13.1, 1.7)	R11	(4.3, 4.3)
R4	(12.1, 2.0)	R12	(3.3, 4.7)
R5	(11.1, 2.1)	R13	(2.3, 5.1)
R6	(10.1, 2.5)	R14	(1.3, 6.3)
R7	(8.3, 2.7)	R15	(0.8, 6.7)
R8	(7.3, 3.1)		

Figure 14: Concert hall model.

positions on the seat. The coordinates are presented in the figure. For TD-FEM, the sound source is a modulated Gaussian pulse with the 2.5 kHz frequency upper-limit. Time responses were calculated up to 2.0 s. However, FD-FEM calculations were performed at 100 Hz – 2.5 kHz with 0.5 Hz intervals, in which the volume acceleration of 1 m^3/s^2 was given to the point source. The concert hall is bounded by frequency-independent absorbing boundaries $\Gamma_{a,1}$ and $\Gamma_{a,2}$, and a frequency-dependent absorbing boundary $\Gamma_{a,3}$. We gave a frequency-independent specific acoustic admittance ratio y_n^r for $\Gamma_{a,1}$ and $\Gamma_{a,2}$. The values for $\Gamma_{a,1}$ and $\Gamma_{a,2}$ are y_n^r=1/71.52 and 1/7.14 respectively corresponding to α_0 of 0.054 and 0.43. Similarly to the office problem, we assumed frequency-dependent specific acoustic admittance ratios of three GWs, i.e., GW24K, GW32K, and GW96K, to $\Gamma_{a,3}$. The setting which was used included virtual values, but the absorption of upholstered chairs is similar to that of porous-type absorbers.

Regarding spatial discretization, we discretized the domain with variously sized irregular shaped elements having maximum edge length of 0.02 m. The resulting mesh has spatial resolution of 6.9 elements per wavelength at the upper-limit frequency. The DOF was 806,748. The Δt used in TD-FEM is set to the stability limit value of 1/49,600 s. The TD-FEM and FD-FEM calculations were done with OpenMP parallel computation using 16 threads. For TD-FEM, the time-marching schemes of Eqs. (16)–(20) were parallelized. FD-FEM solved the linear system of equations at each frequency with parallel sparse direct solver PARDISO. The parallelization parts are the hotspots of calculation with the respective methods.

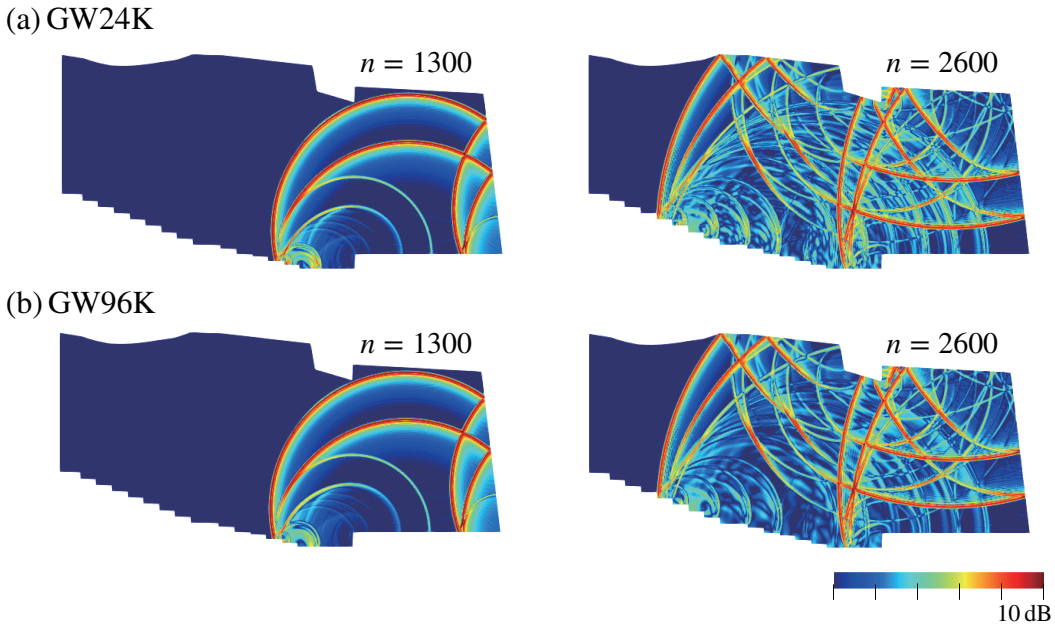

Figure 15: Comparison of SPL distributions in the hall at 1,300 and 2,600 time steps for different seat absorption settings calculated using TD-FEM: (a) GW24K and (b) GW96K.

4.3.2. Results and discussion

Figures 15(a) and 15(b) respectively show SPL distributions in the hall at 1,300 and 2,600 time steps for the two seat absorption settings of GW24K and GW96K. We can find isotropic sound propagations with low dispersion error: the GW96K seat absorption case shows lower reflection SPL from the seat than the GW24K case because of the higher sound-absorption capability.

Figures 16(a) and 16(b) present an SPL comparison at R1 calculated respectively using FD-FEM and TD-FEM for GW96K seat absorption case. The lower panel shows an enlarged view at 2.3–2.5 kHz. Overall, SPLs of the two methods agree very well. The enlarged figure shows that the TD-FEM result calculated with Δt_{crit} converges to the FD-FEM result. We were unable to find any frequency shift at which peaks and dips occur in the concert hall results because the sound field was discretized with elements of various sizes. Therefore, for most elements, Δt_{crit} is a sufficiently small value. Figure 17 shows the critical time intervals in respective elements calculated from the eigenvalue problem $[\boldsymbol{k}_{\mathrm{e}} - (\frac{\omega}{c_0})^2 \boldsymbol{m}_{\mathrm{e}}]\boldsymbol{p}_{\mathrm{e}} = 0$, in which the values are normalized by the stability limit value Δt_{crit}. For most elements,

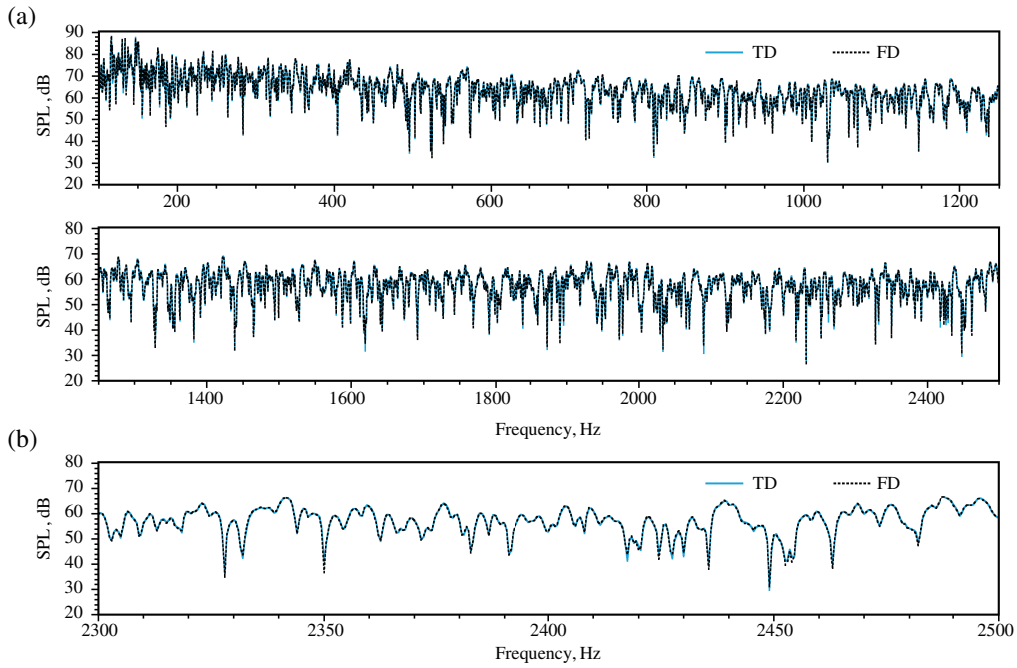

Figure 16: Comparison of SPLs at R1 calculated using FD-FEM (FD) and TD-FEM (TD) for the case with GW96K: (a) frequency response at 100 Hz – 2.5 kHz and (b) enlarged view at 2.3–2.5 kHz.

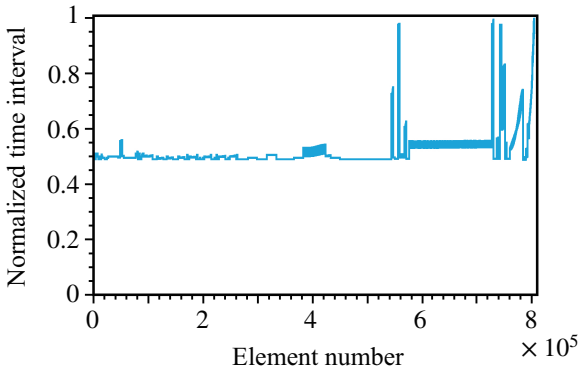

Figure 17: Normalized time interval for all elements.

the normalized time intervals appear to be around 0.5, meaning that stable computation is possible for the elements with a two times larger value of the Δt_{crit}. The results are true for all other receiving point results and for other GW cases.

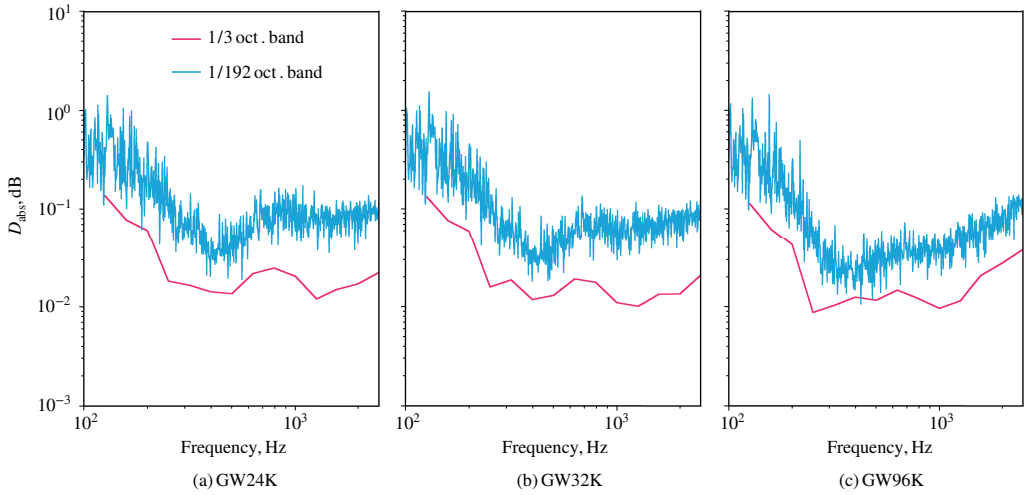

Figure 18: Absolute differences in 1/3 octave band SPL and 1/192 octave band SPL for three seat absorption cases: (a) GW24K, (b) GW32K, and (c) GW96K.

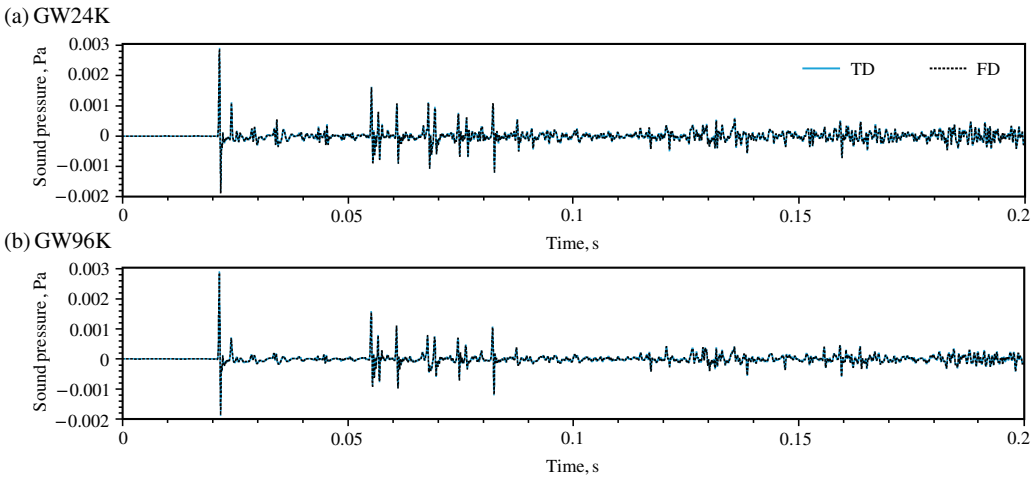

Figure 19: Time responses at R1 in the early time region calculated using FD-FEM and TD-FEM for different seat absorption cases: (a) GW24K and (b) GW32K.

Figures 18(a)– 18(c) show the absolute differences in 1/3 octave band SPL and 1/192 octave band SPL for three seat absorption cases. Larger differences are found, exceeding 1 dB in the 1/192 octave band SPL below 200 Hz. These larger differences are attributable to the same reasons as those in the office model, i.e., large difference at dips. It is negligible for practical

aspects of view. In addition, the absolute difference is less than 1 dB above 200 Hz, indicating that both methods have a similar level of accuracy. A markedly small difference was found below 0.2 dB at all frequencies in the 1/3 octave band SPL comparison.

Figures 19(a) and 19(b) present comparisons of time responses in the early time region up to 0.2 s for the GW24K and GW96K seat absorption cases. For calculation of the time response in FD-FEM, we re-computed the frequency response at frequencies of 0.5 Hz – 7 kHz with a 0.5 Hz interval. In both figures, we can find excellent agreement in the fine structure of the two waveforms. Regarding the waveform similarity, the averaged CC value for all receiving points results exceeds 0.999 for all GW cases. It is further visible that a higher sound absorption effect is obtained for GW96K case, as shown in the visualization result portrayed in Fig. 15.

Finally, we can present higher efficiency of TD-FEM for the acoustic simulation in a large-scale complicated concert hall model. The iterative solver convergence is quite good, with the mean iteration number of 6.0–6.2 per time step. The computational times of TD-FEM are 1,022–1,041 s, which is 17.9–18.2 times faster than 18,592 s for the FD-FEM calculations at 100 Hz – 2.5 kHz with a 0.5 Hz interval. This finding marked hastening of TD-FEM compared to FD-FEM derives from the difference in the scalability of the linear system solver. The diagonally scaled CG solver which was used is inherently more suitable for parallel computations than the direct solver. Furthermore, the required memory in TD-FEM is 220 MBytes, which is much less than 2,455 MBytes of the FD-FEM. However, we must also mention that FD-FEM can be highly efficient when a highly efficient preconditioned iterative solver for solving the linear systems with complex symmetric matrix appeared in large-scale room acoustic problems, which converges rapidly with small iteration numbers and with high parallel scalability while maintaining small non-zero components of coefficient matrix per row, is developed.

5. Conclusions

This paper presented discussion of the effectiveness of the implicit TD-FEM for room acoustic simulations, including frequency-dependent absorbing BCs. For that purpose, we compared the TD-FEM performance with the fourth-order accurate FD-FEM via impedance tube problems and real-scale 2D room acoustic problems. For both problems, we assumed a rigidly backed glass wool sound absorber with three flow resistivity values for frequency-

dependent absorbing BCs. First, the impedance tube problem reveals that the solution convergence rate of TD-FEM approximates to 2, which is the same as in FD-FEM; the TD-FEM solution converges to the FD-FEM solution in the limit $\Delta t \to 0$. Results also show that the error magnitude is dependent on the flow resistivity values of absorbing materials. It becomes larger for higher flow-resistant materials.

A performance comparison in the real-scale 2D acoustic simulations in the office and the concert hall revealed high potential of implicit TD-FEM on room acoustic simulations. Consequently, this study demonstrated that the implicit TD-FEM can predict a broadband time response with considerably lower computational costs than those of FD-FEM while maintaining similar accuracy. Although the presented TD-FEM has an implicit algorithm, the linear system of equations at each time step is solvable easily using the simple diagonal scaled CG solver, which is suitable for parallel computations. Additionally, results demonstrated that the stability condition for frequency-independent absorbing BCs performed well for all numerical experiments undertaken for this study. Therefore, TD-FEM is useful from a stability perspective. Finally, it can be concluded that the TD-FEM including the frequency-dependent impedance BCs has favorable properties for large-scale room acoustic simulations at broad frequencies. The results are expected to be beneficial for FD-FEM users who encounter the difficulties of solving large-scale room acoustic problems in the frequency domain because the presented TD-FEM can be coded directly from FD-FEM with the same spatial discretization mesh.

Future work will be undertaken to present an explicit TD-FEM for room acoustic simulation with frequency-dependent absorbing BCs. Additionally, performance of the implicit TD-FEM including extended-reactive porous sound absorbing model reported in the literature [55] will be demonstrated in comparison with the frequency-domain FEM to demonstrate its effectiveness further.

Appendix A. Rational function parameters of GW

In this appendix, for readers' convenience, parameters y_∞, A_i, B_i, C_i, λ_i, α_i, and β_i for three GWs, which are required for the rational function form of Eq. (10) are given in tabulated form in Table A.1– A.3.

Table A.1: Parameters y_∞, A_i, B_i, C_i, λ_i, α_i, and β_i for GW24K.

y_∞	0.62			
i	1	2	3	4
A_i	-7.47	-37.64	-120.13	421.14
B_i	11221.70	12483.62	27406.57	
C_i	3353.26	1685.22	43162.67	
λ_i	1045.38	2589.19	6032.82	19531.12
α_i	4636.42	7549.83	36049.39	
β_i	-17724.28	-59081.77	-112968.21	

Table A.2: Parameters y_∞, A_i, B_i, C_i, λ_i, α_i, and β_i for GW32K.

y_∞	0.73		
i	1	2	3
A_i	-16.35	-139.97	581.99
B_i	9641.96	11894.52	9455.47
C_i	4965.00	2505.03	39776.29
λ_i	1567.58	4772.52	18858.42
α_i	6581.17	11218.74	40312.52
β_i	-15446.90	-55867.28	-97435.95

Table A.3: Parameters y_∞, A_i, B_i, C_i, λ_i, α_i, and β_i for GW96K.

y_∞	0.92							
i	1	2	3	4	5	6	7	8
A_i	22.98	-34.33	52.81	-99.12	11.36	-13.02	7551.10	-35762.49
B_i	1442.38	6695.05	-4725.50					
C_i	7936.79	7012.75	3140.68					
λ_i	737.82	856.35	1868.09	2523.72	3709.72	8270.16	21302.86	71992.07
α_i	10093.20	22252.28	26736.45					
β_i	-6219.29	-41722.56	-63692.70					

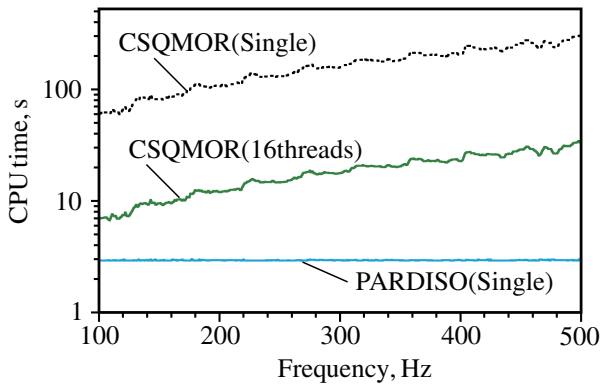

Figure B.20: Comparison of CPU times between PARDISO and CSQMOR, where Single and 16threads respectively represent serial computation and parallel computation with 16 threads.

Appendix B. Selection of linear system solver for FD-FEM

The preliminary study results obtained for the selection of linear system solver for the FD-FEM are shown briefly here. We used the office model with GW32K wall absorber for the selection, in which the performance of the sparse direct solver and CSQMOR iterative solver with a diagonal scaling preconditioning was examined at frequencies of 100 Hz to 500 Hz with 1 Hz interval. The CSQMOR is a recently developed QMR method based on coupled two-term biconjugate A-orthonormalization procedure. The convergence tolerance of CSQMOR was set to 10^{-6}. The computations were performed by serial computation for PARDISO, whereas we performed both serial and parallel computations with 16threads for CSQMOR. Figure B.20 presents a comparison of CPU times among them. Results showed that PARDISO outperforms CSQMOR with less CPU time. Although CSQMOR shows a significant speedup by the parallel computation, PARDISO shows higher performance. For reference, CSQMOR method required 4382-23306 iterations for convergence where the iteration numbers increase at higher frequencies. From the result and because we have available memory sufficient for 2D problems, we chose the sparse direct solver for FD-FEM.

References

[1] Sakamoto S, Nagatomo H, Ushiyama A, Tachibana H. Calculation of impulse responses and acoustic parameters in a hall by the finite-difference

time-domain method. Acoust Sci & Tech 2008;29(4):256–65.

[2] Yasuda Y, Ueno S, Kadota M, Sekine H. Applicability of locally reacting boundary conditions to porous material layer backed by rigid wall: Wave-based numerical study in non-diffuse sound field with unevenly distributed sound absorbing surfaces. Appl Acoust 2016;113:45–57.

[3] Okuzono T, Sakagami K, Otsuru T. Dispersion-reduced time domain FEM for room acoustics simulation. In Proceedings of the 23rd International Congress on Acoustics, Aachen, Germany, 9–13 September 2019.

[4] Yasuda Y, Saito K, Sekine H. Effects of the convergence tolerance of iterative methods used in the boundary element method on the calculation results of sound fields in rooms. Appl Acoust 2020;157:106997.

[5] Hoshi K, Hanyu T, Okuzono T, Sakagami K, Yairi M, Harada S, Takahashi S, Ueda Y. Implementation experiment of a honeycomb-backed MPP sound absorber in a meeting room. Appl Acoust 2020;157:107000.

[6] ISO 3382-1:2009. Acoustics – Measurement of room acoustic parameters – Part 1: Performance spaces.

[7] Botteldooren D. Finite-difference time-domain simulation of low-frequency room acoustics problems. J Acoust Soc Am 1995;98(6):3302–08.

[8] Sakamoto S. Phase-error analysis of high-order finite-difference time-domain scheme and its influence on calculation results of impulse response in closed sound field. Acoust Sci & Tech 2007;28(5):295–309.

[9] Kowalczyk K, Walstijn M. Formulation of locally reacting surfaces in FDTD/K-DWM modelling of acoustic spaces. Acta Acust United Acta 2008;94:891–906.

[10] Kowalczyk K, Van Walstijn M. Room Acoustics Simulation Using 3-D Compact Explicit FDTD Schemes. IEEE Trans Audio Speech Lang Process 2010;19:4–46.

[11] Hamilton B, Bilbao S. FDTD methods for 3-D room acoustics simulation with high-order accuracy in space and time. IEEE Trans Audio Speech Lang Process 2017;25:2112–24.

[12] Toyoda M, Eto D. Prediction of microperforated panel absorbers using the finite-difference time-domain method. Wave Motion 201;86:110–24.

[13] Otsuru T, Okamoto N, Okuzono T, Sueyoshi T. Applications of large-scale finite element sound field analysis onto room acoustics. In Proceedings of the 19th International Congress on Acoustics, Madrid, Spain, 2–7 September 2007.

[14] Okuzono T, Otsuru T, Tomiku R, Okamoto N. Fundamental accuracy of time domain finite element method for sound field analysis of rooms. Appl Acoust 2010;71(10):940–6.

[15] Okuzono T, Otsuru T, Tomiku R, Okamoto N. Application of modified integration rule to time-domain finite element acoustic simulation of rooms. J Acoust Soc Am 2012;132(2):804–13.

[16] Okuzono T, Otsuru T, Tomiku R, Okamoto N. A finite-element method using dispersion reduced spline elements for room acoustics simulation. Appl Acoust 2014;79:1–8.

[17] Yoshida T, Okuzono T, Sakagami K. Time domain room acoustic solver with fourth-order explicit FEM using modified time integration. Appl Sci 2020;10:3750.

[18] Yoshida T, Okuzono T, Sakagami K. Implementation of a frequency-dependent impedance boundary model into a room acoustic solver with time-domain finite element method. Acoust Sci & Technol 2020;41:819–22.

[19] Bilbao S. Modeling of Complex Geometries and Boundary Conditions in Finite Difference/Finite Volume Time Domain Room Acoustics Simulation. IEEE Trans. Audio Speech Lang Process 2013;21:1524–33.

[20] Bilbao S, Hamilton B, Botts J, Savioja L. Finite volume time domain room acoustics simulation under general impedance boundary conditions. IEEE Trans Audio Speech Lang Process 2016;24:161–73.

[21] Hornikx M, Hak C, Wenmaekers R. Acoustic modelling of sports halls, two case studies. J Build Perform Simul 2015;8:26–38.

[22] Hornikx M, Krijnen T, van Harten L. openPTSD: The open source pseudo-spectral time-domain method for acoustic propagation. Comput Phys Communications 2016;203:298–308.

[23] Simonaho SP, Lähivaara T, Huttunen T. Modeling of acoustic wave propagation in time-domain using the discontinuous Galerkin method – A comparison with measurements. Appl Acoust 2012;73:173–83.

[24] Wang H, Sihar I, Pagán Muñoz R, Hornikx M. Room acoustics modelling in the time-domain with the nodal discontinuous Galerkin method. J Acoust Soc Am 2019;145:2650–63.

[25] Wang H, Hornikx M. Time-domain impedance boundary condition modeling with the discontinuous Galerkin method for room acoustics simulations. J Acoust Soc Am 2020;147:2534–46.

[26] Pind F, Jeong CH, Hesthaven JS, Engsig-Karup AP, Strømann-Andersen J. A phenomenological extended-reaction boundary model for time-domain wave-based acoustic simulations under sparse reflection conditions using a wave splitting method. Appl Acoust 2021;172:107596.

[27] Pind F, Engsig-Karup AP, Jeong CH, Hesthaven JS, Mejling MS, Strømann-Andersen J. Time domain room acoustic simulations using the spectral element method. J Acoust Soc Am 2019;145:3299–310.

[28] Mehra R, Raghuvanshi N, Savioja L, Lin MC, Manocha D. An efficient GPU-based time domain solver for the acoustic wave equation. Appl Acoust 2012;73:83–94.

[29] Rabisse K, Ducourneau J, Faiz A, Trompette N. Numerical modelling of sound propagation in rooms bounded by walls with rectangular irregularities and frequency-dependent impedance. J Sound Vib 2019;440:291–314.

[30] Yue B, Guddati MN. Dispersion-reducing finite elements for transient acoustics. J Acoust Soc Am 2005;118(4):2132–41.

[31] Newmark NM. A method of computation for structural dynamics. J Eng Mech Div 1959;85:67–94.

[32] Hughes TJR. "Algorithms for hyperbolic and parabolic-hyperbolic problems", in *The finite element method linear static and dynamic finite element analysis*, Dover, 2000, Chap. 9, pp. 490–569.

[33] Barrett R, Berry M, Chan TF, Demmel J, Donato J, Dongarra J, Eijkhout V, Pozo R, Romine C, van der Vorst H. "Nonstationary iterative methods", in *Templates for the solution of linear systems: Building blocks for iterative methods*, SIAM, Philadelphia, 1994, Chap. 2.3, pp. 14–30.

[34] Okuzono T, Shimizu N, Sakagami K. Predicting absorption characteristics of single-leaf permeable membrane absorbers using finite element method in a time domain. Appl Acoust 2019;151:172–82.

[35] Dragna D, Pineau P, Blanc-Benon P. A generalized recursive convolution method for time-domain propagation in porous media. J Acoust Soc Am 2015;138:1030–42.

[36] Troian R, Dragna D, Bailly C, Galland MA. Broadband linear impedance eduction for multimodal acoustic propagation in the presence of a mean flow. J Sound Vib 2017;392:200–216.

[37] Otsuru T, Tomiku R, Toyomasu M, Takahashi Y. Finite element sound field analysis of rooms in built environment. In Proceedings of the Eighth International Congress on Acoustics, Hong Kong, China, 2–6 July 2001.

[38] Okamoto N, Tomiku R, Otsuru T, Yasuda Y. Numerical analysis of large-scale sound fields using iterative methods part II: Application of Krylov subspace methods to finite element analysis. J Comput Acoust 2007;15:473–93.

[39] Aretz M, Vorländer M. Combined wave and ray based room acoustic simulations of audio systems in car passenger compartments, Part II: Comparison of simulations and measurements. Appl Acoust 2014;76:52–65.

[40] Okuzono T, Sakagami K. A frequency domain finite element solver for acoustic simulations of 3D rooms with microperforated panel absorbers. Appl Acoust 2018;129:1–12.

[41] Barrett R, Berry M, Chan TF, Demmel J, Donato J, Dongarra J, Eijkhout V, Pozo R, Romine C, van der Vorst H. "Data structures", in *Templates for the solution of linear systems: Building blocks for iterative methods*, SIAM, Philadelphia, 1994, Chap. 4.3, pp. 64–76.

[42] ISO 10534-2:1998. Acoustics – Determination of sound absorption coefficient and impedance in impedance tubes – Part 2: Transfer-function method.

[43] Allard JF, Atalla N. "Acoustic impedance at normal incidence of fluids. Substitution of a fluid layer for a porous layer", in *Propagation of Sound in Porous Media: Modeling Sound Absorbing Materials*, Second ed.; John Wiley & Sons, Ltd.: Chichester, UK, 2009; pp. 15–27.

[44] Guddati MN, Yue B. Modified integration rules for reducing dispersion error in finite element methods. Comput Methods Appl Mech Engrg 2004;193:275–87.

[45] Miki Y. Acoustical properties of porous materials – Modifications of Delany–Bazley models. J Acoust Soc Jpn 1990;11:19–24.

[46] Gustavsen B, Semlyen A. Rational approximation of frequency domain responses by vector fitting. IEEE Trans Pow Del 1999;14:1052–61.

[47] Okuzono T, Sakagami K. Dispersion error reduction of absorption finite elements based on equivalent fluid model. Acoust Sci & Technol 2018;39:362–65.

[48] Okuzono T, Mohamed MS, Sakagami K. Potential of room acoustic solver with plane-wave enriched finite element method. Appl Sci 2020;10:1969.

[49] Zhang J, Dai H. A new quasi-minimal residual method based on a biconjugate A-orthonormalization procedure and coupled two-term recurrences. Numer Algor 2015;70:875–96.

[50] van der Vorst HA, Melissen J. A Petrov–Galerkin type method for solving $Ax{=}b$, where A is symmetric complex. IEEE Trans Magn 1990;26(2):706–8.

[51] Sogabe T, Zhang SL. A COCR method for solving complex symmetric linear systems. J Comput Appl Math 2007;199:297–303.

[52] Freund RW, Nachtigal NM. An implementation of the QMR method based on coupled two-term recurrences. SIAM J Sci Stat Comput 1994;15(2):313–37.

[53] Lam YW. Issues for computer modeling of room acoustics in non-concert hall settings. Acoust Sci & Technol 2005;26:145–55.

[54] Jeong CH, Ih JG. Effects of source and receiver locations in predicting room transfer functions by a phased beam tracing method. J Acoust Soc Am 2012;131:3864–75.

[55] Yoshida T, Okuzono T, Sakagami K. Time-domain finite element formulation of porous sound absorbers based on an equivalent fluid model. Acoust Sci & Technol 2020;41:837–40.